

Total Deep Variation: A Stable Regularizer for Inverse Problems

Erich Kobler, Alexander Effland, Karl Kunisch and Thomas Pock

June 17, 2020

Abstract

Various problems in computer vision and medical imaging can be cast as inverse problems. A frequent method for solving inverse problems is the variational approach, which amounts to minimizing an energy composed of a data fidelity term and a regularizer. Classically, handcrafted regularizers are used, which are commonly outperformed by state-of-the-art deep learning approaches. In this work, we combine the variational formulation of inverse problems with deep learning by introducing the data-driven general-purpose total deep variation regularizer. In its core, a convolutional neural network extracts local features on multiple scales and in successive blocks. This combination allows for a rigorous mathematical analysis including an optimal control formulation of the training problem in a mean-field setting and a stability analysis with respect to the initial values and the parameters of the regularizer. In addition, we experimentally verify the robustness against adversarial attacks and numerically derive upper bounds for the generalization error. Finally, we achieve state-of-the-art results for numerous imaging tasks.

1 Introduction

The statistical viewpoint of linear inverse problems accounts for measurement uncertainties and loss of information in the observations z in a rigorous framework. Bayes' theorem states that the posterior probability $p(x|z)$ is proportional to the product of the data likelihood $p(z|x)$ and the prior $p(x)$, i.e.

$$p(x|z) \propto p(z|x)p(x),$$

and represents the belief in a distinct solution x given z . Typically, solutions are computed by maximizing the posterior probability, which yields the maximum a posterior (MAP) estimator. In a negative log-domain, the MAP estimator amounts to minimizing the variational problem

$$E(x, z) := D(x, z) + R(x),$$

where the data fidelity term D is identified with the negative log-likelihood $-\log p(z|x)$ and the regularizer R corresponds to the negative log of the prior distribution $-\log p(x)$. In this paper, we assume that the observations are generated by a linear inverse problem of the form

$$z = Ay + \xi,$$

where y is the unknown ground truth, A is a known task-dependent linear operator and ξ is additive noise. For example, A is the identity matrix in the case of denoising, and it is a downsampling operator

in the case of single image super-resolution. While the data fidelity term is straightforward to model, there has been much effort to design a regularizer that captures the complexity of the statistics of natural images.

A classical and widely used regularizer is the total variation (TV) originally proposed in [44], which is based on the first principle assumption that images are piecewise constant with sparse gradients. A well-known caveat of the sparsity assumption of TV is the formation of clearly visible artifacts known as staircasing effect. To overcome this problem, the first principle assumption has later been extended to piecewise smooth images incorporating higher order image derivatives such as infimal convolution based models [6] or the total generalized variation [5]. Inspired by the fact that edge continuity plays a fundamental role in the human visual perception, regularizers penalizing the curvature of level lines have been proposed in [8, 9, 38]. While these regularizers are mathematically well-understood, the complexity of natural images is only partially reflected in their formulation. For this reason, hand-crafted variational methods have nowadays been largely outperformed by purely data-driven methods as predicted by Levin and Nadler [28] a decade ago.

It has been recognized quite early that a proper statistical modeling of regularizers should be based on learning [58], which has recently been advocated e.g. in [29, 30]. One of the most successful early approaches is the Fields of Experts (FoE) regularizer [43], which can be interpreted as a generalization of the total variation, but builds upon learned filters and learned potential functions. While the FoE prior was originally learned generatively, it was shown in [45] that a discriminative learning via implicit differentiation yields improved performance. A computationally more feasible method for discriminative learning is based on unrolling a finite number of iterations of a gradient descent algorithm [13]. Additionally using iteration dependent parameters in the regularizer was shown to significantly increase the performance (TNRD [11], [27]). In [26], variational networks (VNs) are proposed, which give an incremental proximal gradient interpretation of TNRD. Interestingly, such truncated schemes are not only computationally much more efficient, but are also superior in performance with respect to the full minimization. A continuous time formulation of this phenomenon was proposed in [15] by means of an optimal control problem, within which an optimal stopping time is learned.

An alternative approach to incorporate a regularizer into a proximal algorithm, known as plug-and-play prior [51] or regularization by denoising [41], is the replacement of the proximal operator by an existing denoising algorithm such as BM3D [12]. Combining this idea with deep learning was proposed in [33, 40, 53]. However, all aforementioned schemes lack a variational structure and are thus not interpretable in the framework of MAP inference.

The significance of stability for data-driven methods has recently been addressed in [3], in which a systematical treatment of adversarial attacks for inverse problems was performed. This issue has been studied in the context of classification by [46], where adversarial samples have been introduced. These samples are computed by perturbing input images as little as possible such that the attacked algorithm predicts wrong labels. Incorporating adversarial samples in the training process of data driven methods increases their robustness as studied in [46]. In recent years, several methods were proposed for generating adversarial examples such as the fast gradient sign method [17], Deepfool [35] or universal adversarial perturbations [34]. In the context of inverse problems, adversarial examples are typically computed by maximizing the norm difference between the output of an algorithm and the associated ground truth in a local neighborhood around an input. Thus, the robustness w.r.t. adversarial attacks of an algorithm depends to a large extent on the local Lipschitz constant of the mapping defined by the algorithm.

This paper is an extended version of the prior conference proceeding [25], in which a novel data-driven regularizer termed *Total Deep Variation (TDV)* is introduced. The TDV regularizer is inspired

by recent design patterns of state-of-the-art deep convolutional neural networks and simultaneously ensures a variational structure. We achieve this by representing the total energy of the regularizer by means of a residual multi-scale network (Figure 1) leveraging smooth activation functions. Our proposed TDV regularizer can be used as a generic regularizer in variational formulations of linear inverse problems. In analogy to [15, 25], we minimize an energy composed of a data fidelity term and the TDV regularizer using a gradient flow emanating from the corrupted input image on a finite time horizon $[0, T]$ for a stopping time T , where the terminal state of the gradient flow defines the reconstructed image. Then, the stopping time and the parameters of the TDV regularizer are computed by solving a mean-field optimal control problem as advocated in [14], in which the cost functional is defined as the expectation of the loss function with respect to a training data distribution. The state equation of the optimal control problem is a stochastic ordinary differential equation coinciding with the gradient flow of the energy, where the only source of randomness is the initial state. We prove the existence of minimizers for this optimal control problem using the direct method in the calculus of variations. A semi-implicit time discretization of the gradient flow results in a discretized optimal control problem in the mean-field setting, for which we also prove the existence of minimizers as well as a first order necessary condition to automatize the computation of the optimal stopping time. This training process is a form of *discriminative learning* because we directly learn the functional form of the negative log-posterior [37], in which the TDV regularizer can be interpreted as a *discriminative prior*. In fact, the learned TDV regularizer adapts to the specific imaging task as we show in the eigenfunction analysis. Moreover, the particular recursive structure of the discrete gradient flow allows the derivation of a stability analysis with respect to the initial states and the learned TDV parameters. Both estimates depend on the local Lipschitz constant of the TDV regularizer, which is estimated in the mean-field setting. Several numerical experiments demonstrate the applicability of the proposed method to numerous image restoration problems, in which we obtain state-of-the-art results. In particular, we examine the robustness of this approach against perturbations and adversarial attacks, and an upper bound for the generalization error is empirically computed.

The major contributions of this paper are as follows:

- the design of a novel generic multi-scale variational regularizer learned from data,
- a rigorous mathematical analysis including a mean-field optimal control formulation of the learning problem,
- a stability analysis of the proposed method, which is validated by numerical experiments,
- a nonlinear eigenfunction analysis for the visualization and understanding of the learned regularizer,
- numerical evaluation of the robustness against adversarial attacks and empirical upper bounds for the generalization error,
- state-of-the-art results on a number of classical image restoration and medical image reconstruction problems with an impressively low number of learned parameters.

As already mentioned above, this paper extends the conference paper [25] in several aspects. First, we extend the optimal control problem to a mean-field perspective including existence theorems. Second, a rigorous stability analysis is pursued and numerical experiments regarding the robustness are performed. Finally, we add several experiments involving color denoising, a multi-channel eigenfunction analysis, and numerical experiments addressing the robustness against adversarial attacks.

Let $x \in \mathbb{R}^n$. We denote by $\|x\|_2 := \sqrt{\sum_{i=1}^n x_i^2}$ the ℓ^2 -norm of x and by $\|x\|_\infty := \max_{i=1, \dots, n} |x_i|$ its ℓ^∞ -norm. Further, $A^\top \in \mathbb{R}^{n \times m}$ denotes the matrix transpose of $A \in \mathbb{R}^{m \times n}$. For two Banach

spaces \mathcal{X} and \mathcal{Y} , we denote by $C^0(\mathcal{X}, \mathcal{Y})$ the space of continuous functions mapping from \mathcal{X} to \mathcal{Y} , and by $C^k(\mathcal{X}, \mathcal{Y})$ for $k \geq 1$ the space of k -times continuously differentiable functions from \mathcal{X} to \mathcal{Y} . Finally, we denote by $D_s f$ the Jacobian of the function f w.r.t. the s^{th} argument.

2 Mean-Field Optimal Control Problem

In this section, we cast the training process as a mean-field optimal control problem taking into account the general approach presented in [14].

Let $(\mathcal{Y} \times \Xi, \mathcal{F}, \mathbb{P})$ be a complete probability space on $\mathcal{Y} \times \Xi$ with σ -algebra \mathcal{F} and probability measure \mathbb{P} . We denote by (y, ξ) a pair of independent random variables modeling the data representing the *ground truth image* $y \in \mathcal{Y} \subset \mathbb{R}^{n_C}$ and *additive noise* $\xi \in \Xi \subset \mathbb{R}^l$ with associated distribution denoted by $\mathcal{T} = \mathcal{T}_{\mathcal{Y}} \times \mathcal{T}_{\Xi}$. Each ground truth image y represents an image of size $n = n_1 \times n_2$ with C channels and is related to the additive noise ξ by means of the *observation*

$$z = Ay + \xi,$$

where $A \in \mathbb{R}^{l \times n_C}$ is a fixed task-dependent linear operator of this linear inverse problem. In particular, we assume that both \mathcal{Y} and Ξ are compact sets, which implies that all observations are contained in a compact set $\mathcal{Z} \subset \mathbb{R}^l$. To estimate the unknown ground truth image y from the observation z we pursue a variational approach, which amounts to minimizing the energy functional

$$E(x, z, \theta) := D(x, z) + R(x, \theta) \tag{1}$$

among all $x \in \mathbb{R}^{n_C}$. In this paper, we consider the squared ℓ^2 -data fidelity term $D(x, z) = \frac{1}{2} \|Ax - z\|_2^2$ and the total deep variation [25] regularizer R , which is a convolutional neural network depending on learned training parameters $\theta \in \Theta$, where $\Theta \subset \mathbb{R}^p$ is compact and convex (the exact structure of the network is discussed below).

Let $\tilde{x} \in C^1([0, T], \mathbb{R}^{n_C})$ be an *image trajectory*, which evolves according to the *gradient flow equation* [2] associated with (1) on a finite time interval $(0, T)$ given by

$$\begin{aligned} \dot{\tilde{x}}(t) &= -D_1 E(\tilde{x}(t), z, \theta) = f(\tilde{x}(t), z, \theta) \\ &:= -A^\top (A\tilde{x}(t) - z) - D_1 R(\tilde{x}(t), \theta) \end{aligned} \tag{2}$$

for $t \in (0, T)$ and $x(0) = x_0$. Here, the observation-dependent initial value x_0 is computed as $x_0 = A_{\text{init}} z$ for a fixed task-dependent matrix $A_{\text{init}} \in \mathbb{R}^{n_C \times l}$, which could be, for instance, the pseudoinverse of A . The proper choice of the stopping time $T \in [0, T_{\text{max}}]$ for a fixed $T_{\text{max}} > 0$ is essential for the quality of the reconstruction $\tilde{x}(T)$ of y . A more feasible, yet equivalent gradient flow is derived from the reparametrization $x(t) = \tilde{x}(tT)$, which yields for $t \in (0, 1)$

$$\dot{x}(t) = Tf(x(t), z, \theta) \tag{3}$$

with the same initial value as before. We frequently write $x(t, y, \xi, T, \theta)$ to highlight the dependency of the image trajectory on the parameters $(y, \xi, T, \theta) \in \mathcal{Y} \times \Xi \times [0, T_{\text{max}}] \times \Theta$ for given $t \in [0, 1]$. In particular, $x(1, y, \xi, T, \theta)$ is the computed output image.

In what follows, the training process is described as a *mean-field optimal control problem* [14] with control parameters θ and T . To this end, let $\ell \in C^1(\mathbb{R}^{n_C}, \mathbb{R}_0^+)$ be a convex and coercive *loss function*. Then, we define the *cost functional* as

$$J(T, \theta) := \mathbb{E}_{(y, \xi) \sim \mathcal{T}} [\ell(x(1, y, \xi, T, \theta) - y)],$$

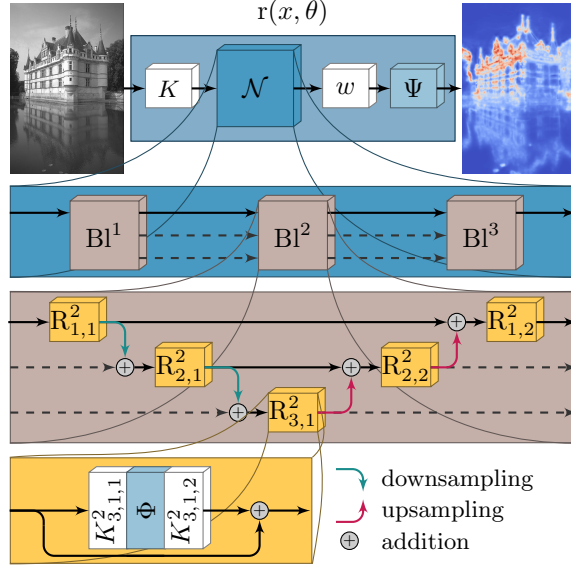


Figure 1: The network structure of the total deep variation with 3 blocks each operating on 3 scales.

which results in the mean-field optimal control problem

$$\inf_{T \in [0, T_{\max}], \theta \in \Theta} J(T, \theta). \quad (4)$$

Remark 1. The mean-field optimal control formulation already encompasses the *sampled optimal control problem*. In detail, given a finite training set $(y^i, \xi^i)_{i=1}^N \sim \mathcal{T}^N$ drawn from the data distribution we can define the *discrete probability measure* as $\mathbb{P}(y, \xi) = \frac{1}{N} \sum_{i=1}^N \delta[y = y^i] \delta[\xi = \xi^i]$, where $\delta[s = t] = 1$ if $s = t$ and 0 otherwise. This particular choice results in the sampled cost functional

$$J(T, \theta) = \frac{1}{N} \sum_{i=1}^N \ell(x(1, y^i, \xi^i, T, \theta) - y^i).$$

In this paper, the regularizer $R : \mathbb{R}^{nC} \times \Theta \rightarrow \mathbb{R}$ is modeled as the total deep variation originally proposed in [25], which is the sum of the pointwise deep variation $r : \mathbb{R}^{nC} \times \Theta \rightarrow \mathbb{R}^n$, i.e.

$$R(x, \theta) = \sum_{i=1}^n r(x, \theta)_i.$$

The pointwise deep variation is defined as

$$r(x, \theta) = \Psi(w\mathcal{N}(Kx)),$$

where

- $K \in \mathbb{R}^{nm \times nC}$ is the matrix representation of a learned 3×3 convolution kernel for $m = 32$ feature channels with zero-mean constraint, i.e. $\sum_{i=1}^{nC} K_{j,i} = 0$ for $j = 1, \dots, n$, which implies a spatial and radiometrical shift-invariance,

- $\mathcal{N} : \mathbb{R}^{nm} \rightarrow \mathbb{R}^{nm}$ is a multiscale convolutional neural network as illustrated in Figure 1, where we assume that $\|D\mathcal{N}\|_{C^0(\mathbb{R}^{nm})} \leq C_{\mathcal{N}}(\theta)$,
- $w \in \mathbb{R}^{n \times nm}$ is a learned 1×1 convolution kernel,
- $\Psi : \mathbb{R}^n \rightarrow \mathbb{R}^n, (x_1, \dots, x_n) \mapsto (\psi(x_1), \dots, \psi(x_n))$ using the *potential function* $\psi \in C^2(\mathbb{R}, \mathbb{R})$ satisfying $\|D\Psi\|_{C^0(\mathbb{R}^n)} \leq C_{\Psi}$ for a constant $C_{\Psi} > 0$.

We denote by θ the entity of learned parameters, i.e. K , w and all convolution kernels of \mathcal{N} . Following [25], the total deep variation TDV_a^b for integers $a, b \geq 1$ consists of b blocks $\text{Bl}^1, \dots, \text{Bl}^b$ (gray blocks in Figure 1), each of them has a U-Net [42] type architecture, where on all a scales residual blocks $\text{R}_{1,1}^i, \text{R}_{1,2}^i, \dots, \text{R}_{a-1,1}^i, \text{R}_{a-1,2}^i, \text{R}_{a,1}^i$ (yellow blocks in Figure 1) are applied. To increase the expressiveness of the network, residual connections are added between scales of consecutive blocks whenever possible. Each residual block $\text{R}_{j,k}^i$ with $i \in \{1, \dots, b\}$, $j \in \{1, \dots, a\}$ and $k \in \{1, 2\}$ exhibits the particular structure $\text{R}_{j,k}^i(x, \theta) = x + K_{j,k,2}^i \Phi(K_{j,k,1}^i x)$ for convolution operators $K_{j,k,1}^i, K_{j,k,2}^i \in \mathbb{R}^{nm \times nm}$ of size 3×3 with m feature channels and no bias. Following [21], the log-student-t-distribution is a suitable model for the statistics of natural images, that is why we choose the particular activation function $\Phi : \mathbb{R}^{nm} \rightarrow \mathbb{R}^{nm}, (x_1, \dots, x_{nm}) \mapsto (\phi(x_1), \dots, \phi(x_{nm}))$ using the component-wise function $\phi(x) = \frac{1}{2} \log(1 + x^2)$ with the properties $\phi'(0) = 0$ and $\phi''(0) = 1$. Taking into account the work by Zhang [56], we use 3×3 convolutions and transposed convolutions with stride 2 for downsampling and upsampling in conjunction with a blur kernel to avoid aliasing.

The existence of solutions to the mean-field optimal control problem is established in the next theorem.

Theorem 2.1. *The minimum in (4) is attained.*

Proof. The particular structure of the proposed total deep variation results in the estimate

$$\begin{aligned} \|D_1 \text{R}(x, \theta)\|_2 &= \|K^\top D\mathcal{N}(Kx)w^\top D\Psi(w\mathcal{N}(Kx))\|_2 \\ &\leq \|K\|_2 \|D\mathcal{N}(Kx)\|_2 \|w\|_2 \|D\Psi(w\mathcal{N}(Kx))\|_2 \\ &\leq \|K\|_2 C_{\mathcal{N}}(\theta) \|w\|_2 C_{\Psi} =: C_{\text{R}}(\theta) \end{aligned}$$

for all $x \in \mathbb{R}^{nC}$ and all $\theta \in \Theta$, where we used that $\|D\Psi\|_{C^0(\mathbb{R}^n)} \leq C_{\Psi}$ and $\|D\mathcal{N}\|_{C^0(\mathbb{R}^{nm})} \leq C_{\mathcal{N}}(\theta)$. In detail, the convolutional neural network is a complex concatenation of residual blocks, where the gradient of each of these blocks can be estimated as

$$\|D_1 \text{R}_{j,k}^i(x, \theta)\|_2 = \|\text{Id} + (K_{j,k,1}^i)^\top D\Phi(K_{j,k,1}^i x) K_{j,k,2}^i\|_2 \quad (5)$$

for $x \in \mathbb{R}^{nm}$. In particular, (5) can be uniformly bounded independently of x due to $\sup_{x \in \mathbb{R}} |\phi'(x)| = \frac{1}{2}$. Then, the right-hand side of the state equation can be bounded as follows:

$$\|Tf(x, z, \theta)\|_2 \leq T(\|A\|_2 \|z\|_2 + C_{\text{R}}(\theta) + \|A\|_2^2 \|x\|_2) \quad (6)$$

for $z \in \mathbb{R}^l$. This affine growth already ensures that the maximum domain of existence of the state equation (3) coincides with \mathbb{R} [49, Theorem 2.17]. As a further result, we obtain that $x \in C^1([0, 1], C^0(\mathcal{Y} \times \Xi \times [0, T_{\max}] \times \Theta, \mathbb{R}^{nC}))$ due to the smoothness of the regularizer and

$$x(t, y, \xi, T, \theta) \in \mathcal{X}$$

for all $(t, y, \xi, T, \theta) \in [0, 1] \times \mathcal{Y} \times \Xi \times [0, T_{\max}] \times \Theta$ for a compact and convex set $\mathcal{X} \subset \mathbb{R}^{nC}$.

Let $(T^j, \theta^j) \in [0, T_{\max}] \times \Theta$ be a minimizing sequence for J with an associated state $x^j := x(\cdot, \cdot, \cdot, T^j, \theta^j) \in C^1([0, 1], C^0(\mathcal{Y} \times \Xi, \mathbb{R}^{nC}))$. The compactness of $[0, T_{\max}] \times \Theta$ implies that there exists a subsequence (not relabeled) such that $(T^j, \theta^j) \rightarrow (T^*, \theta^*) \in [0, T_{\max}] \times \Theta$. In what follows, we prove that x^j converges to $x^* := x(\cdot, \cdot, \cdot, T^*, \theta^*) \in C^1([0, 1], C^0(\mathcal{Y} \times \Xi, \mathbb{R}^{nC}))$ in $C^0([0, 1] \times \mathcal{Y} \times \Xi)$. We denote by L_x and L_θ the Lipschitz constants of D_1R w.r.t. x and θ , i.e.

$$\begin{aligned} \|D_1R(x, \theta) - D_1R(\tilde{x}, \theta)\|_2 &\leq L_x \|x - \tilde{x}\|_2, \\ \|D_1R(x, \theta) - D_1R(x, \tilde{\theta})\|_2 &\leq L_\theta \|\theta - \tilde{\theta}\|_2 \end{aligned}$$

for all $x, \tilde{x} \in \mathcal{X}$ and all $\theta, \tilde{\theta} \in \Theta$. Then, we can estimate for any $(y, \xi) \in \mathcal{Y} \times \Xi$ and $z = Ay + \xi$ as follows:

$$\begin{aligned} &\|T^* f(x^*(t, y, \xi), z, \theta^*) - T^j f(x^j(t, y, \xi), z, \theta^j)\|_2 \\ &\leq |T^* - T^j| \left(\|A\|_2^2 \max_{x \in \mathcal{X}} \|x\|_2 + \|A\|_2 \max_{z \in \mathcal{Z}} \|z\|_2 + \max_{(x, \theta) \in \mathcal{X} \times \Theta} \|D_1R(x, \theta)\|_2 \right) \\ &\quad + T_{\max} L_\theta \|\theta^* - \theta^j\|_2 + T_{\max} (\|A\|_2^2 + L_x) \|x^*(t, y, \xi) - x^j(t, y, \xi)\|_2 \\ &=: C_T |T^* - T^j| + C_\theta \|\theta^* - \theta^j\|_2 + C_x \|x^*(t, y, \xi) - x^j(t, y, \xi)\|_2. \end{aligned}$$

Hence, since all state equations satisfy the initial condition $x^*(0, z) = x^j(0, z) = A_{\text{init}}z$, we can apply Gronwall's inequality for initial value problems [49, Theorem 2.8] to obtain

$$\|x^*(t, y, \xi) - x^j(t, y, \xi)\|_2 \leq \frac{C_T |T^* - T^j| + C_\theta \|\theta^* - \theta^j\|_2}{C_x} (e^{C_x t} - 1).$$

Thus, we can deduce the uniform convergence of x^j to x^* in $C^0([0, 1] \times \mathcal{Y} \times \Xi)$ as $j \rightarrow \infty$, which implies $\lim_{j \rightarrow \infty} J(T^j, \theta^j) = J(T^*, \theta^*)$. \square

3 Discretization of the Optimal Control Problem

In this section, we propose a numerical time discretization scheme for the mean-field optimal control problem discussed in the previous section. For an a priori fixed number of iteration steps $S \in \mathbb{N}$, we propose a semi-implicit discretization of the state equation (3), which yields

$$x_{s+1} = x_s - \frac{T}{S} A^\top (Ax_{s+1} - z) - \frac{T}{S} D_1R(x_s, \theta) \in \mathbb{R}^{nC} \quad (7)$$

for $s = 0, \dots, S-1$ and initial state $x_0 = A_{\text{init}}z \in \mathbb{R}^{nC}$. This equation is equivalent to $x_{s+1} = g(x_s, z, T, \theta)$ with

$$g(x, z, T, \theta) := (\text{Id} + \frac{T}{S} A^\top A)^{-1} (x + \frac{T}{S} (A^\top z - D_1R(x, \theta))).$$

We denote by $\hat{x}_s(y, \xi, T, \theta)$ the state of this discretization at time s given the ground truth y , the additive noise ξ , the stopping time T and the parameters θ . Note that the smoothness of the regularizer and the compactness of $\mathcal{Y}, \Xi, [0, T_{\max}]$ and Θ directly imply that

$$\hat{x} : \mathcal{Y} \times \Xi \times [0, T_{\max}] \times \Theta \rightarrow \mathcal{X}^{S+1} \subset (\mathbb{R}^{nC})^{S+1}$$

for a compact and convex set \mathcal{X} . Then, the *discretized mean-field optimal control problem* is given by

$$\inf_{T \in [0, T_{\max}], \theta \in \Theta} J_S(T, \theta), \quad (8)$$

where the discrete cost functional reads as

$$J_S(T, \theta) := \mathbb{E}_{(y, \xi) \sim \mathcal{T}} [\ell(\widehat{x}_S(y, \xi, T, \theta) - y)].$$

Theorem 3.1. *The minimum in (8) is attained.*

Proof. Let $(T^j, \theta^j) \in [0, T_{\max}] \times \Theta$ be a minimizing sequence for J_S with an associated state $\widehat{x}^j := \widehat{x}(\cdot, \cdot, T^j, \theta^j)$. As in the time continuous case, the compactness of $[0, T_{\max}] \times \Theta$ implies the existence of a subsequence (again not relabeled) such that $(T^j, \theta^j) \rightarrow (T^*, \theta^*) \in [0, T_{\max}] \times \Theta$, where the associated state is given by $\widehat{x}^* := \widehat{x}(\cdot, \cdot, T^*, \theta^*)$. Then, we can estimate for any $(y, \xi) \in \mathcal{Y} \times \Xi$ and $s = 0, \dots, S-1$ as follows:

$$\|\widehat{x}_{s+1}^*(y, \xi) - \widehat{x}_{s+1}^j(y, \xi)\|_2 \leq C_T |T^* - T^j| + C_\theta \|\theta^* - \theta^j\|_2 + C_x \|\widehat{x}_s^*(y, \xi) - \widehat{x}_s^j(y, \xi)\|_2.$$

Note that the constants C_T , C_θ and C_x depend on A , S , L_x , L_θ , T_{\max} , Θ and \mathcal{Z} . An induction argument reveals

$$\|\widehat{x}_{s+1}^*(y, \xi) - \widehat{x}_{s+1}^j(y, \xi)\|_2 \leq (C_T |T^* - T^j| + C_\theta \|\theta^* - \theta^j\|_2) \frac{1 - C_x^{s+1}}{1 - C_x}.$$

In particular, $\|x_S^* - x_S^j\|_{C^0(\mathcal{Y} \times \Xi)} \rightarrow 0$ as $j \rightarrow \infty$, which implies $\lim_{j \rightarrow \infty} J_S(T^j, \theta^j) = J_S(T^*, \theta^*)$. \square

The existence of the discrete adjoint state is discussed in the subsequent theorem:

Theorem 3.2. *Let $(T^*, \theta^*) \in [0, T_{\max}] \times \Theta$ be a pair of control parameters for J_S and $x^* \in \mathcal{L} := L^2(\mathcal{Y} \times \Xi, (\mathbb{R}^{n_C})^{S+1})$ the corresponding state. Then there exists a discrete adjoint state $p^* \in \mathcal{L}$ given by*

$$p_s^*(y, \xi) = (\text{Id} - \frac{T^*}{S} D_1^2 \mathbf{R}(x_s^*(y, \xi), \theta^*)) (\text{Id} + \frac{T^*}{S} A^\top A)^{-1} p_{s+1}^*(y, \xi) \quad (9)$$

for $s = S-1, \dots, 0$ with terminal condition $p_S^*(y, \xi) = -D\ell(x_S^*(y, \xi) - y)$.

Proof. First, we define the functional $G : \mathcal{L} \times [0, T_{\max}] \times \Theta \rightarrow \mathcal{L}$ representing the constraints as follows:

$$G(x, T, \theta)(y, \xi) = \begin{pmatrix} x_0(y, \xi) - A_{\text{init}}(Ay + \xi) \\ x_1(y, \xi) - g(x_0(y, \xi), Ay + \xi, T, \theta) \\ \vdots \\ x_S(y, \xi) - g(x_{S-1}(y, \xi), Ay + \xi, T, \theta) \end{pmatrix}.$$

Then, the Lagrange functional $L : \mathcal{L} \times [0, T_{\max}] \times \Theta \times \mathcal{L} \rightarrow \mathbb{R}$ using $\mathcal{L}^* \cong \mathcal{L}$ is given by

$$L(x, T, \theta, p) := \mathbb{E}_{(y, \xi) \sim \mathcal{T}} \left[\ell(x_S(y, \xi) - y) + \sum_{s=0}^S \langle p_s(y, \xi), G_s(x(y, \xi), T, \theta) \rangle \right].$$

Following [52, Theorem 43.D], the Lagrange multiplier $p^* \in \mathcal{L}$ associated with (x^*, T^*, θ^*) exists if ℓ and G are (continuously) Frechét differentiable and $D_1 G(x^*, T^*, \theta^*)$ is surjective. The differentiability

requirements are immediately implied by the smoothness requirements of R. To prove the surjectivity of D_1G , we first compute for $x \in \mathcal{L}$

$$D_1G(x^*, T^*, \theta^*)(x)(y, \xi) = \begin{pmatrix} x_0(y, \xi) \\ x_1(y, \xi) - D_1g(x_0^*(y, \xi), Ay + \xi, T^*, \theta^*)x_0(y, \xi) \\ \vdots \\ x_S(y, \xi) - D_1g(x_{S-1}^*(y, \xi), Ay + \xi, T^*, \theta^*)x_{S-1}(y, \xi) \end{pmatrix}.$$

Thus, for any $w \in \mathcal{L}$ the solution $x \in \mathcal{L}$ of the equation $D_1G(x^*, T^*, \theta^*)(x) = w$ is given by

$$\begin{aligned} x_0(y, \xi) &= w_0(y, \xi), \\ x_s(y, \xi) &= w_s(y, \xi) + D_1g(x_{s-1}^*(y, \xi), Ay + \xi, T^*, \theta^*)x_{s-1}(y, \xi) \end{aligned}$$

for $s = 1, \dots, S$, which proves the surjectivity and thus the existence of Lagrange multipliers. Finally, (9) is implied by the optimality of L w.r.t. x . \square

Next, we derive an optimality condition for the stopping time, which can easily be evaluated numerically.

Theorem 3.3. *Let (T^*, θ^*) be a stationary point of J_S with associated state x^* and adjoint state p^* as in Theorem 3.2. Then,*

$$\mathbb{E}_{(y, \xi) \sim \mathcal{T}} \left[\sum_{s=0}^{S-1} \left\langle p_{s+1}^*(y, \xi), (\text{Id} + \frac{T^*}{S} A^* A)^{-1} (x_{s+1}^*(y, \xi) - x_s^*(y, \xi)) \right\rangle \right] = 0. \quad (10)$$

Proof. Let us define $B(T) := \text{Id} + \frac{T}{S} A^* A$ and observe that

$$\frac{d}{dT} (B(T)^{-1}) = -B(T)^{-1} \left(\frac{d}{dT} B(T) \right) B(T)^{-1}.$$

The derivative of g w.r.t. T reads as

$$\begin{aligned} \frac{d}{dT} g(x, z, T, \theta) &= -B(T)^{-1} \left(\frac{1}{S} A^\top AB(T)^{-1} (x + \frac{T}{S} (A^\top z - D_1R(x, \theta))) - \frac{1}{S} (A^\top z - D_1R(x, \theta)) \right) \\ &= -\frac{1}{T} B(T)^{-1} \left(x - B(T)^{-1} (x + \frac{T}{S} (A^\top z - D_1R(x, \theta))) \right). \end{aligned}$$

Due to (7) the following relation holds true for the optimal $x^* \in \mathcal{L}$ and $s = 0, \dots, S-1$:

$$B(T)x_{s+1}^* = x_s^* + \frac{T}{S} (A^\top z - D_1R(x_s^*, \theta)).$$

Hence, the optimality condition of L w.r.t. T^* reads as

$$\mathbb{E}_{(y, \xi) \sim \mathcal{T}} \left[-\frac{1}{T^*} \sum_{s=0}^{S-1} \left\langle p_{s+1}^*(y, \xi), (\text{Id} + \frac{T^*}{S} A^* A)^{-1} (x_{s+1}^*(y, \xi) - x_s^*(y, \xi)) \right\rangle \right] = 0,$$

which proves this theorem. \square

4 Stability Analysis

Here, we examine the stability of the proposed method, which quantifies the changes in the output caused by local perturbations of the observations and training parameters, respectively. The central assumption in both cases is that the distribution of the test data coincides with the distribution of the training data in the mean-field setting. Numerical results for the stability analysis are presented in subsection 5.7.

4.1 Stability Analysis w.r.t. Input

In what follows, we perform a stability analysis for the proposed algorithm, in which we derive upper bounds along the trajectories for different noise instances in the mean-field context. To this end, we first compute quantiles of the Lipschitz constant of the explicit update for the proposed discretization scheme given the data distribution \mathcal{T} . Then, upper bounds for the difference of trajectories associated with one ground truth image and different noise instances drawn from the data distribution are derived using a recursion argument.

Let $x, \tilde{x} \in \mathbb{R}^{nC}$, $T \in [0, T_{\max}]$, and $\theta \in \Theta$. We define the local Lipschitz constant of the explicit update step $x \mapsto x - \frac{T}{S} D_1 \mathbf{R}(x, \theta)$ as

$$L_x(x, \tilde{x}, T, \theta) := \frac{\|x - \frac{T}{S} D_1 \mathbf{R}(x, \theta) - \tilde{x} + \frac{T}{S} D_1 \mathbf{R}(\tilde{x}, \theta)\|_2}{\|x - \tilde{x}\|_2},$$

where we set $L_x = 0$ if the denominator vanishes. Then, the cumulative distribution function F_S of the local Lipschitz constant on the data distribution \mathcal{T} for $L \in \mathbb{R}$ is defined as

$$F_S(L) = \mathbb{P}\left(\max_{s=0, \dots, S} L_x(\hat{x}_s(y, \xi, T, \theta), \hat{x}_s(y, \tilde{\xi}, T, \theta), T, \theta) \leq L : y \sim \mathcal{T}_y, \xi, \tilde{\xi} \sim \mathcal{T}_\Xi\right).$$

Thus, the maximum local Lipschitz constant of the explicit update step along each trajectory is bounded by $F_S^{-1}(1 - \delta)$ with probability $1 - \delta$.

Theorem 4.1 (Stability w.r.t. input). *Let $(T, \theta) \in [0, T_{\max}] \times \Theta$ be fixed control parameters, $y \sim \mathcal{T}_y$ and $\xi, \tilde{\xi} \sim \mathcal{T}_\Xi$. We denote by $x, \tilde{x} \in (\mathbb{R}^{nC})^{S+1}$ two solutions of the state equation associated with $z = Ay + \xi$ and $\tilde{z} = Ay + \tilde{\xi}$, and corresponding $x_0 = A_{\text{init}}z$ and $\tilde{x}_0 = A_{\text{init}}\tilde{z}$, respectively. The discrete state equations are given by*

$$x_{s+1} = g(x_s, z, T, \theta), \quad \tilde{x}_{s+1} = g(\tilde{x}_s, \tilde{z}, T, \theta)$$

for $s = 0, \dots, S - 1$. Let $\delta \in [0, 1)$,

$$\alpha_1(\delta) := \|B^{-1}\|_2 F_S^{-1}(1 - \delta), \quad \beta_1 := \frac{T}{S} \|B^{-1}\|_2 \|A\|_2$$

for $B := \text{Id} + \frac{T}{S} A^\top A$. Then,

$$\frac{1}{nC} \|x_{s+1} - \tilde{x}_{s+1}\|_2 \leq \frac{1}{nC} \left(\alpha_1(\delta)^{s+1} \|A_{\text{init}}\|_2 + \frac{1 - \alpha_1(\delta)^{s+1}}{1 - \alpha_1(\delta)} \beta_1 \right) \|z - \tilde{z}\|_2$$

holds true with probability $1 - \delta$.

Proof. The definition of the semi-implicit scheme (7) implies that for any $s = 0, \dots, S-1$ the inequality

$$\|x_{s+1} - \tilde{x}_{s+1}\|_2 \leq \|B^{-1}\|_2 (F_S^{-1}(\delta)\|x_s - \tilde{x}_s\|_2 + \frac{T}{S}\|A\|_2\|z - \tilde{z}\|_2)$$

holds true with probability $1 - \delta$. By taking into account a recursion argument, the geometric series formula $\sum_{i=0}^n q^i = \frac{1-q^{n+1}}{1-q}$, and the estimate $\|x_0 - \tilde{x}_0\|_2 \leq \|A_{\text{init}}\|_2\|z - \tilde{z}\|_2$ we obtain the desired result. \square

4.2 Stability Analysis w.r.t. Parameters

Next, we elaborate on the stability of the proposed approach w.r.t. variations of the learned parameters $\theta \in \Theta$. To this end, we estimate the local Lipschitz constants of the TDV regularizer w.r.t. both of its arguments in the mean-field setting to derive upper bounds along the trajectories emanating from the same initial state, but with different parameters θ and $\tilde{\theta}$. In detail, the perturbed parameters $\tilde{\theta}$ is drawn from a uniform distribution supported on a component-wise relative ϵ -ball around θ . A recursion argument involving the estimated Lipschitz constants results in computable upper bounds for the norm difference along trajectories associated with θ and $\tilde{\theta}$.

Let $B_\epsilon(\theta)$ be the component-wise relative ϵ -ball around $\theta = (K, K_{j,k,1}^i, K_{j,k,2}^i, w) \in \Theta$ w.r.t the ℓ^∞ -norm, i.e.

$$B_\epsilon(\theta) = \left\{ \tilde{\theta} = (\tilde{K}, \tilde{K}_{j,k,1}^i, \tilde{K}_{j,k,2}^i, \tilde{w}) \in \Theta : \begin{aligned} \|\tilde{K} - K\|_\infty &\leq \epsilon \|K\|_\infty, \|\tilde{K}_{j,k,1}^i - K_{j,k,1}^i\|_\infty \leq \epsilon \|K_{j,k,1}^i\|_\infty, \\ \|\tilde{K}_{j,k,2}^i - K_{j,k,2}^i\|_\infty &\leq \epsilon \|K_{j,k,2}^i\|_\infty, \|\tilde{w} - w\|_\infty \leq \epsilon \|w\|_\infty \end{aligned} \right\}.$$

Further, we denote by $\text{proj}_\Theta : \mathbb{R}^p \rightarrow \Theta$ the orthogonal projection onto Θ , and by $\mathcal{U}(S)$ the uniform distribution for any set $S \subset \mathbb{R}^p$. Then, the cumulative distribution function $F_{S,x}$ of the local Lipschitz constant of the regularizer w.r.t. its first component is given as

$$F_{S,x}(L) = \mathbb{P}\left(\max_{s=0,\dots,S} L_x(\hat{x}_s(y, \xi, T, \theta), \hat{x}_s(y, \xi, T, \tilde{\theta}), T, \theta) \leq L : (y, \xi) \sim \mathcal{T}, \tilde{\theta} \sim \mathcal{U}(\text{proj}_\Theta(B_\epsilon(\theta)))\right)$$

for $L \in \mathbb{R}$. Likewise, we define the local Lipschitz constant of TDV w.r.t. its second argument as

$$F_{S,\theta}(L) = \mathbb{P}\left(\max_{s=0,\dots,S} L_\theta(\hat{x}_s(y, \xi, T, \tilde{\theta}), \theta, \tilde{\theta}) \leq L : (y, \xi) \sim \mathcal{T}, \tilde{\theta} \sim \mathcal{U}(\text{proj}_\Theta(B_\epsilon(\theta)))\right)$$

for $L \in \mathbb{R}$, where

$$L_\theta(x, \theta, \tilde{\theta}) := \frac{\|D_1\text{R}(x, \theta) - D_1\text{R}(x, \tilde{\theta})\|_2}{\|\theta - \tilde{\theta}\|_2}.$$

Taking into account the above definitions we can state the stability theorem w.r.t. the learned parameters as follows:

Theorem 4.2 (Stability w.r.t. parameters). *Let $T \in [0, T_{\text{max}}]$, $\theta \in \Theta$ and $\tilde{\theta} \sim \mathcal{U}(\text{proj}_\Theta(B_\epsilon(\theta)))$. We denote by $z = Ay + \xi$ an observation associated with $(y, \xi) \sim \mathcal{T}$, and by $\{x_s\}_{s=0}^S, \{\tilde{x}_s\}_{s=0}^S \in (\mathbb{R}^{nC})^{S+1}$ two states satisfying (7) with initial conditions $x_0 = \tilde{x}_0 = A_{\text{init}}z$ and control parameters (T, θ) and $(T, \tilde{\theta})$, respectively. Then, the inequality*

$$\frac{1}{nC} \|x_{s+1} - \tilde{x}_{s+1}\|_2 \leq \frac{1}{nC} \frac{1 - \alpha_2(\delta)^{s+1}}{1 - \alpha_2(\delta)} \beta_2(\delta) \|\theta - \tilde{\theta}\|_2 \quad (11)$$

holds true with probability $1 - \delta$ for $\delta \in [0, 1)$, where

$$\alpha_2(\delta) = \|B^{-1}\|_2 F_{S,x}^{-1}(1 - \frac{\delta}{2}), \quad \beta_2(\delta) = \|B^{-1}\|_2 \frac{T}{S} F_{S,\theta}^{-1}(1 - \frac{\delta}{2})$$

for $B := \text{Id} + \frac{T}{S} A^\top A$.

Proof. Again, using the definition of g yields

$$\|x_{s+1} - \tilde{x}_{s+1}\|_2 \leq \alpha_2(\delta) \|x_s - \tilde{x}_s\|_2 + \beta_2(\delta) \|\theta - \tilde{\theta}\|_2$$

with probability $1 - \delta$, where we exploited

$$\|\mathbb{R}(x_s, \theta) - \mathbb{R}(\tilde{x}_s, \tilde{\theta})\|_2 \leq F_{S,x}^{-1}(1 - \frac{\delta}{2}) \|x_s - \tilde{x}_s\|_2 + F_{S,\theta}^{-1}(1 - \frac{\delta}{2}) \|\theta - \tilde{\theta}\|_2.$$

By exploiting a recursion argument and noting that the initial states coincide the theorem follows. \square

Hence, this theorem provides a computable upper bound for the norm difference of two states w.r.t. perturbations of the TDV parameters. In particular, if (T, θ) is a local minimizer of the cost functional (8), then the stability analysis quantifies the robustness of the trajectories.

5 Numerical Results

In this section, we present numerical results for additive Gaussian denoising, medical reconstruction, and single image super-resolution. To get an intuition for the local behavior of the learned TDV regularizer, we pursue a nonlinear eigenfunction analysis. Moreover, we perform a stability analysis including adversarial attacks and worst case generalization error estimates to demonstrate the robustness of the proposed method.

5.1 Training Details

In all experiments, we use the BSDS400 dataset [31] for training, which determines the discrete probability measure according to Remark 1. Thus, the control parameters (T, θ) are computed by minimizing the *discretized sampled optimal control problem*

$$\min_{T \in [0, T_{\max}], \theta \in \Theta} \frac{1}{N} \sum_{i=1}^N \ell(\hat{x}_S(y^i, \xi^i, T, \theta) - y^i),$$

where $\ell(x) = \|x\|_2^2$ for Gaussian denoising and $\ell(x) = \sum_{i=1}^{nC} \sqrt{x_i^2 + \epsilon^2}$ for single image super-resolution with $\epsilon = 0.01$. We augment data of patch size 93×93 by randomly flipping the images horizontally or vertically, and by rotating the images by multiples of 90° . The ADAM optimizer [24] is employed with a mini batch size of 32 using 10^5 iterations, $\beta_1 = 0.9$ and $\beta_2 = 0.999$, where the initial learning rate $4 \cdot 10^{-4}$ is halved every 25000 iterations. The noise ξ is drawn randomly in each iteration.

5.2 Additive Gaussian Denoising

As a first task, we consider additive Gaussian denoising implying $A = \text{Id} \in \mathbb{R}^{nC \times nC}$, $\xi \sim \mathcal{N}(0, \sigma^2 \text{Id})$ and $l = nC$ for $C = 1$ (gray-scale images) or $C = 3$ (color images).

Table 1: Different possible choices for potential functions ψ evaluated on gray-scale Gaussian denoising ($\sigma = 25$).

ψ	$\ln \cosh(x)$	$\frac{1}{2} \log(1 + x^2)$	x
PSNR	29.3596	29.3662	29.3722

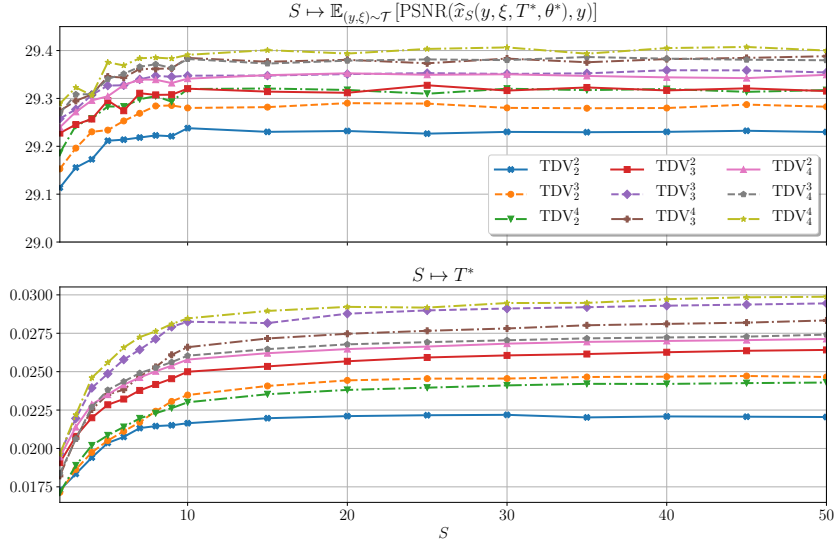


Figure 2: Expected PSNR value and optimal stopping time depending on S for various TDV regularizers (gray-scale Gaussian denoising, $\sigma = 25$).

In the first experiments, we perform an ablation study of the number of blocks b , the number of scales a and the potential function. To this end, we evaluate the performance of the resulting TDV regularizers for additive gray-scale Gaussian denoising by computing the expected PSNR value on the BSDS68 dataset. Figure 2 depicts the expected PSNR values (top) and the optimal stopping times (bottom) as functions of the depth S for color-coded TDV regularizers with $a, b \in \{2, 3, 4\}$. In all cases, the performance increases until $S \approx 10$, beyond this point the curves saturate. Thus, in all subsequent experiments the TDV regularizer is trained for $S = 10$. Moreover, the expected PSNR values increase with the number of learnable parameters, which is correlated with the number of blocks and scales. However, beyond a certain complexity the performance increase saturates, that is why we use the TDV_3^3 regularizer in all further experiments.

Table 1 lists the PSNR values for three possible choices of the potential functions. It turns out that the simplest potential function $\psi(x) = x$, which is neither bounded nor coercive, performs slightly better than the other potential functions. For this reason, we use $\psi(x) = x$ in all further experiments.

In what follows, we discuss the importance of the stopping time for the quality of the output image. To this end, we plot the PSNR values of all BSDS68 test images and the corresponding expected PSNR value (red line) as a function of the stopping time (Figure 3, top). All curves approximately peak around the same optimal stopping time $T^* = 0.172$, which is also identified by the first order condition of

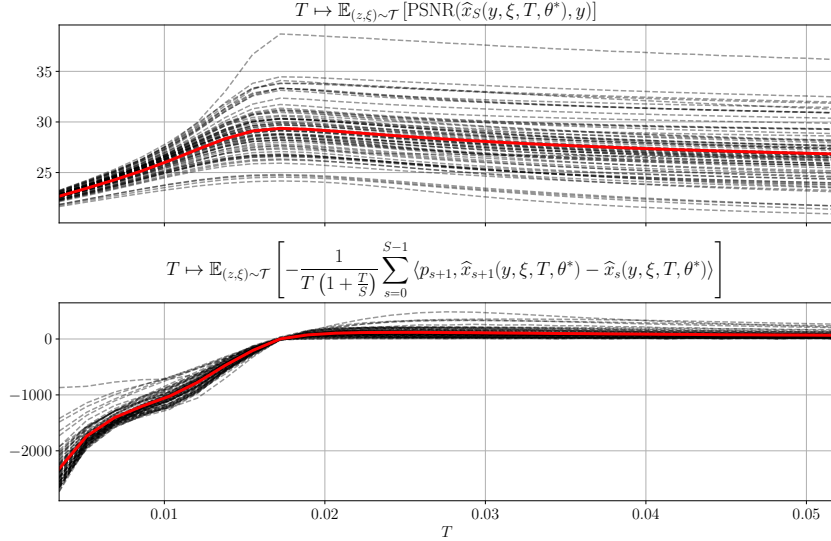


Figure 3: First order optimality condition of the stopping time for gray-scale Gaussian denoising ($\sigma = 25$) using TDV_3^3 and the BSDS68 dataset.

Theorem 3.3 (Figure 3, bottom). Further, Figure 4 presents sequences of output images for gray-scale and color Gaussian denoising trained for $S = 10$ to visually verify the importance of the proper choice of the optimal stopping time. Starting from the noisy input image x_0 (second column), the noise level is gradually decreased until the output image x_{10} (fourth column) is obtained. Beyond this point, the algorithm generates oversmoothed images and details are lost.

A quantitative comparison of expected PSNR values for additive gray-scale and color Gaussian denoising for $\sigma \in \{15, 25, 50\}$ on various image datasets is listed in Table 2 and Table 3. In the $\text{TDV}_{3,25}^3$ column, the PSNR values of our proposed TDV regularizer with three macro-blocks on three scales solely trained for $\sigma = 25$ are presented. To apply the $\text{TDV}_{3,25}^3$ model to different noise levels, we first rescale the noisy images $\bar{x}_{\text{init}} = \bar{z} = \frac{25}{\sigma}z$, then apply the learned scheme (7), and obtain the results via $x_S = \frac{\sigma}{25}\bar{x}_S$. In the last column of Table 2, the PSNR values of the TDV regularizer—*individually* trained for each noise level—are listed. For color Gaussian denoising we only present results obtained by $\text{TDV}_{3,25}^3$ to follow the evaluation standard of the related methods. We achieve state-of-the-art results for gray-scale and color image denoising compared with models of similar complexity. Only FOCNet [22] performs slightly better for gray-scale images at the expense of more than hundred times more trainable parameters. Finally, the TDV regularizers yield higher PSNR values if its parameters are individually optimized for each noise level.

5.3 Computed Tomography Reconstruction

To demonstrate the broad applicability of the proposed TDV regularizer, we perform a two-dimensional computed tomography (CT) reconstruction using the $\text{TDV}_{3,25}^3$ regularizer, which was trained for gray-scale Gaussian image denoising and $S = 10$. We stress that the regularizer is applied *without* any additional training of the TDV parameters.

The task of computed tomography is the reconstruction of an image given a set of projection

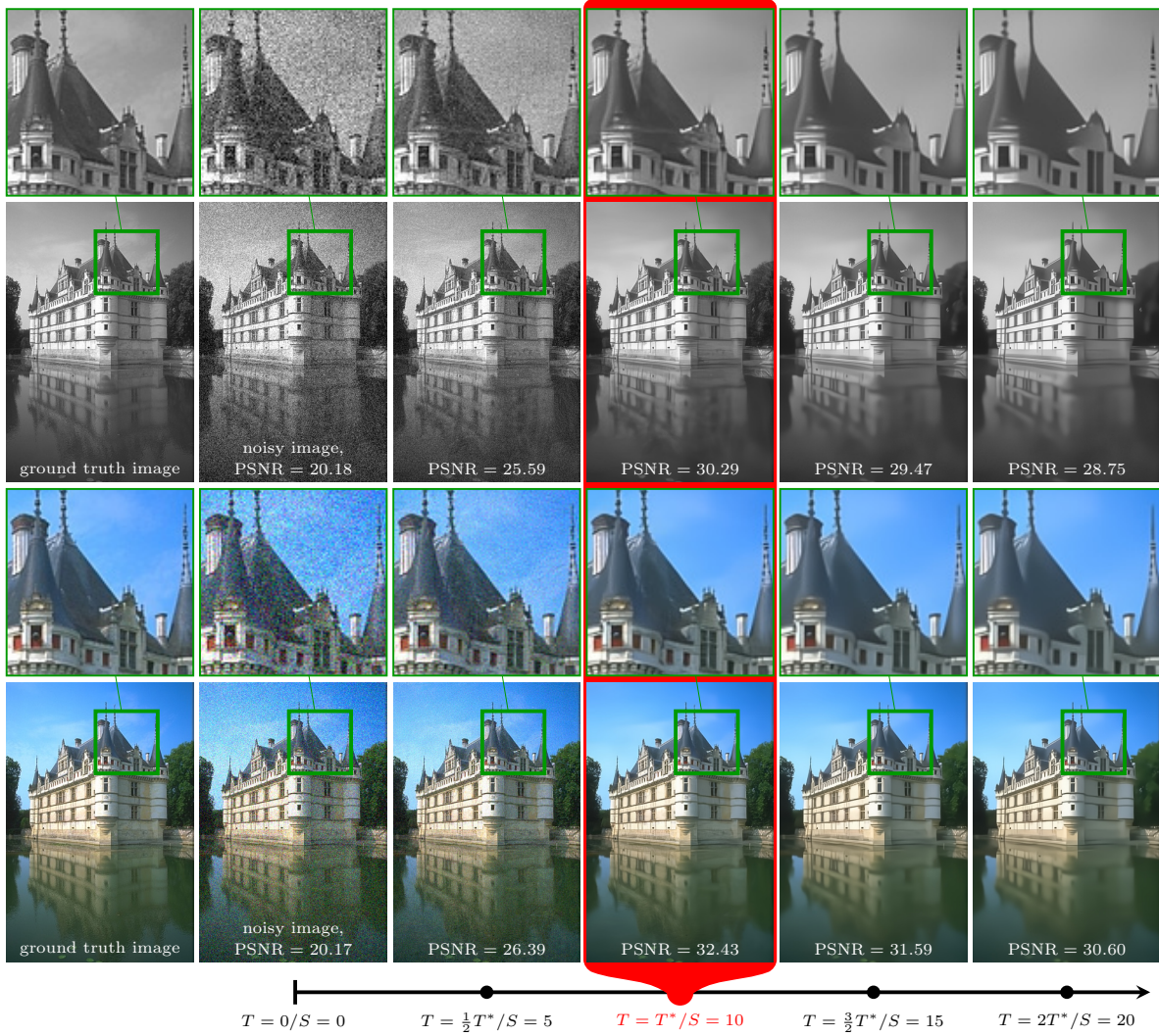


Figure 4: From left to right: Ground truth, noisy input with noise level $\sigma = 25$ and resulting output of TDV_3^3 for $(S, T) \in \{(5, \frac{1}{2}T^*), (10, T^*), (15, \frac{3}{2}T^*), (20, 2T^*)\}$ for Gaussian denoising of gray-scale images (top) and color images (bottom). Note that the best images are framed in red and are obtained at the optimal stopping time, which is $T^* = 0.172$ for gray-scale denoising and $T^* = 0.0247$ for color denoising.

Table 2: Comparison of expected PSNR values for additive gray-scale Gaussian denoising for $\sigma \in \{15, 25, 50\}$ on various image datasets.

Dataset	σ	BM3D [12]	TNRD [11]	DnCNN [54]	FFDNet [55]	N ³ Net [39]	FOCNet [22]	TDV _{3,25} ³	TDV ₃ ³
Set12	15	32.37	32.50	32.86	32.75	-	33.07	32.93	33.02
	25	29.97	30.05	30.44	30.43	30.55	30.73	30.68	30.68
	50	26.72	26.82	27.18	27.32	27.43	27.68	27.52	27.59
BSDS68	15	31.08	31.42	31.73	31.63	-	31.83	31.76	31.84
	25	28.57	28.92	29.23	29.19	29.30	29.38	29.37	29.37
	50	25.60	25.97	26.23	26.29	26.39	26.50	26.42	26.45
Urban100	15	32.34	31.98	32.67	32.43	-	33.15	32.66	32.91
	25	29.70	29.29	29.97	29.92	30.19	30.64	30.38	30.38
	50	25.94	25.71	26.28	26.52	26.82	27.40	26.94	27.04
# Parameters			26,645	555,200	484,800	705,895	53,513,120	387,394	387,394

Table 3: Comparison of expected PSNR values for additive color Gaussian denoising for $\sigma \in \{15, 25, 50\}$ on various image datasets.

Dataset	σ	BM3D [12]	CDnCNN [54]	FFDNet [55]	TDV _{3,25} ³
CBSDS68	15	33.52	33.89	33.87	34.12
	25	30.71	31.23	31.21	31.53
	50	27.38	27.92	27.96	28.26
Kodak24	15	34.28	34.48	34.63	35.01
	25	31.68	32.03	32.13	32.59
	50	28.46	28.85	28.98	29.44
McMaster	15	34.06	33.44	34.66	34.55
	25	31.66	31.51	32.35	32.47
	50	28.51	28.61	29.18	29.41
# Parameters			668,803	852,108	387,970

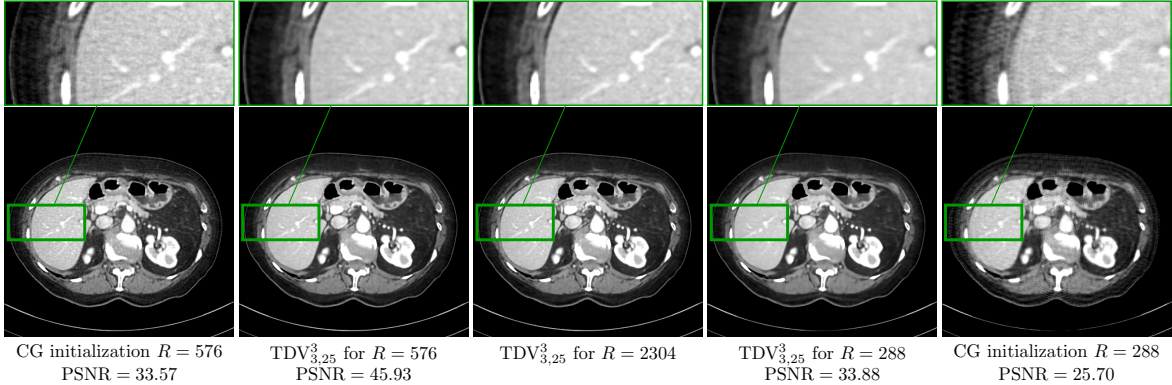


Figure 5: Conjugate gradient reconstruction for 4/8-fold angular undersampled CT task (first/fifth image), results obtained by using the $\text{TDV}_{3,25}^3$ regularizer with $\lambda = 500 \cdot 10^3$ for 4-fold (second image) and $\lambda = 10^6$ for 8-fold undersampling (fourth image), and fully sampled reference reconstruction using the $\text{TDV}_{3,25}^3$ regularizer with $\lambda = 125 \cdot 10^3$ (third image).

measurements called sinogram, in which the detectors of the CT scanner measure the intensity of attenuated X-ray beams. Here, we use the linear attenuation model introduced in [18], where the attenuation is proportional to the intersection area of a triangle, which is spanned by the X-ray source and a detector element, and the area of an image element. In detail, the sinogram z of an image x is computed by $z = A_R x$, where $A_R \in \mathbb{R}^{l \times n}$ is the lookup-table based area integral operator of [18] for R angles and 768 projections implying $l = 768 \cdot R$. Typically, a fully sampled acquisition consists of 2304 angles. For this task, we consider the problem of angular undersampled CT [10], where only a fraction of the angles are measured. We use a 4-fold ($R = 576$) and 8-fold ($R = 288$) angular undersampling to reconstruct a representative image of the MAYO dataset [32] with $n = 768 \times 768$. To account for an imbalance of regularization and data fidelity, we manually scale the data fidelity term by $\lambda > 0$, i.e.

$$D(x, z) := \frac{\lambda}{2} \|A_R x - z\|_2^2.$$

The resulting smooth variational problem is optimized using accelerated gradient descent with Lipschitz backtracking using 1000 steps as discussed in [7].

We present qualitative and quantitative results for CT reconstruction in Figure 5 for a single abdominal CT image. As an initialization, we perform 50 steps of a conjugate gradient method on the data fidelity term (first and last column). Using the proposed $\text{TDV}_{3,25}^3$ regularizer, we are able to suppress the undersampling artifacts while preserving, for instance, the fine vessels in the liver. This highlights that the learned regularizer can be effectively applied as a generic regularizer for linear inverse problems without any transfer learning, which is a particular benefit of the variational structure of the proposed approach.

5.4 Magnetic Resonance Imaging Reconstruction

In what follows, the flexibility of our regularizer $\text{TDV}_{3,25}^3$ learned for denoising and $S = 10$ is shown for accelerated magnetic resonance imaging (MRI) *without* any further adaption of θ .

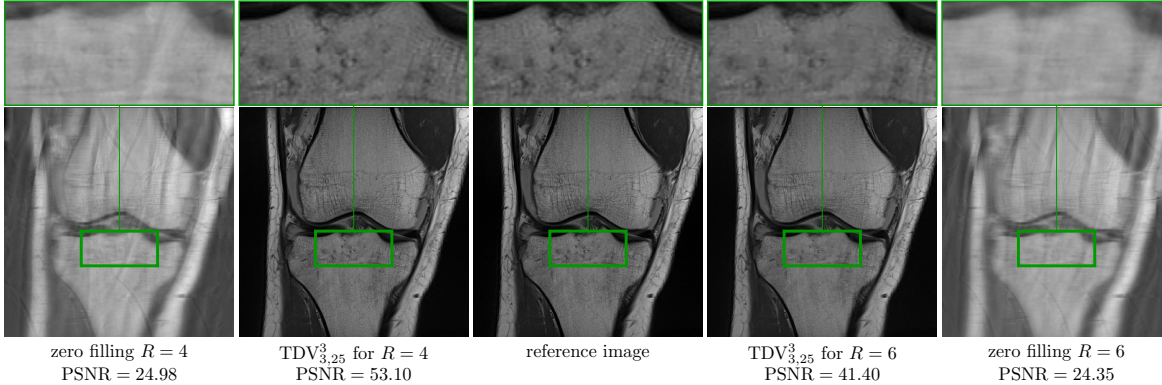


Figure 6: Zero filling initialization for acceleration factors $R \in \{4, 6\}$ (first/fifth image), output using the $\text{TDV}_{3,25}^3$ regularizer with $\lambda = 1000$ for $R = 4$ (second image) and $\lambda = 1500$ for $R = 6$ (fourth image), and fully sampled reference (third image).

In accelerated MRI, k-space data $\{z_i\}_{i=1}^{N_C} \subset \mathbb{C}^n$ is acquired using N_C parallel coils, each measuring a fraction of the full k-space to reduce acquisition time [19]. Here, we use the data fidelity term

$$D(x, \{z_i\}_{i=1}^{N_C}) = \frac{\lambda}{2} \sum_{i=1}^{N_C} \|M_R F C_i x - z_i\|_2^2,$$

where $\lambda > 0$ is a manually adjusted weighting parameter, $M_R \in \mathbb{R}^{n \times n}$ is a binary mask for R -fold Cartesian undersampling, $F \in \mathbb{C}^{n \times n}$ is the discrete Fourier transform, and $C_i \in \mathbb{C}^{n \times n}$ are sensitivity maps, which are estimated using ESPIRiT [50]. For further details we refer the reader to [19]. We use 4-fold and 6-fold Cartesian undersampled MRI data to reconstruct a sample knee image. Again, we minimize the resulting variational energy by accelerated gradient descent with Lipschitz backtracking using 1000 steps [7].

We perform an evaluation of the proposed approach on a representative slice of an undersampled MRI knee acquisition. The slice has a resolution of $n = 320 \times 320$ and $N_C = 15$ receiver coils were used during the acquisition. Figure 6 depicts qualitative results and PSNR values for the reconstruction of 4-fold and 6-fold undersampled k-space data. The first and last columns show the initial images obtained by applying the adjoint operator to the undersampled data. In the second and fourth column we depict the results obtained using $\text{TDV}_{3,25}^3$. Although the TDV regularizer was not trained to account for undersampling artifacts, almost all artifacts are removed in the reconstructions and only some details in the bone are lost. This highlights the versatility and effectiveness of the proposed TDV regularizer since both CT and MRI reconstruction can be properly addressed *without* any fine-tuning of the learned parameters.

5.5 Single Image Super-resolution

In this subsection, we present numerical results for single image super-resolution (SISR). Here, the linear operator $A \in \mathbb{R}^{n_C/\gamma^2 \times n_C}$ is given as a downsampling operator, where $\gamma \in \{2, 3, 4\}$ denotes the scale factor. In detail, its adjoint operator coincides with MATLAB[®]'s bicubic upsampling operator

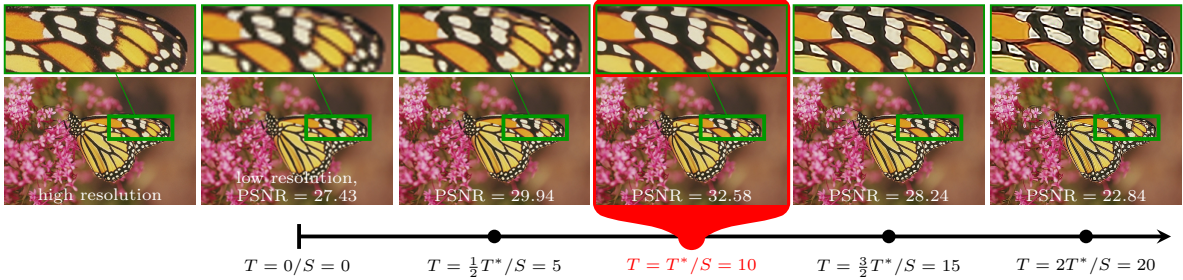


Figure 7: From left to right: High resolution ground truth image, low resolution image with $\gamma = 4$ and $\sigma = 0$, and resulting output of TDV_3^3 for $(S, T) \in \{(5, \frac{1}{2}T^*), (10, T^*), (15, \frac{3}{2}T^*), (20, 2T^*)\}$, where the optimal stopping time is $T^* = 0.043$. Note that the best image is framed in red.

Table 4: PSNR values of various state-of-the-art networks for single image super-resolution ($\sigma = 0$) with a comparable number of parameters.

Dataset	Scale	MemNet [48]	VDSR [23]	DnCNN-3 [54]	DRRN [47]	OISR-LF-s [20]	TDV_3^3
Set14	$\times 2$	33.28	33.03	33.03	33.23	33.62	33.35
	$\times 3$	30.00	29.77	29.81	29.96	30.35	29.94
	$\times 4$	28.26	28.01	28.04	28.21	28.63	28.41
BSDS100	$\times 2$	32.08	31.90	31.90	32.05	32.20	32.17
	$\times 3$	28.96	28.82	28.85	28.95	29.11	28.96
	$\times 4$	27.40	27.29	27.29	27.38	27.60	27.55
# Parameters		585,435	665,984	666,561	297,000	1,370,000	387,970

`imresize`, which is an implementation of a scale factor-dependent interpolation convolution kernel in conjunction with a stride. Since this restoration problem substantially differs from Gaussian image denoising, the parameters of the TDV regularizer have to be optimized for this task individually.

Let nC be a multiple of γ^2 and $y \in \mathbb{R}^{nC}$ be a full resolution ground truth image patch uniformly drawn from the BSDS400 dataset. The observations $z = Ay + \xi \in \mathbb{R}^{nC/\gamma^2}$ used for training are corrupted by additive Gaussian noise ξ with $\sigma \in \{0, 7.65\}$. For the initialization we set $A_{\text{init}} = \gamma A^\top$. The proximal map $(\text{Id} + \frac{T}{S} A^\top A)^{-1}$ is efficiently computed in Fourier space as advocated in [57]. Here, all results are obtained by training a TDV_3^3 regularizer for each scale factor individually.

We compare our SISR results with numerous state-of-the-art networks of similar complexity and list expected PSNR values of the Y-channel in the YCbCr color space over test datasets in Table 4. For the BSDS100 dataset, our proposed method achieves similar results as OISR-LF-s [20] with only one third of the trainable parameters. Figure 7 depicts a restored sequence of images for SISR with scale factor 4 using TDV_3^3 for a representative sample image of the Set14 dataset. Starting from the low resolution initial image, interfaces are gradually sharpened and the best quality is achieved for $T = T^*$. Beyond this point, interfaces are artificially intensified.

5.6 Eigenfunction Analysis

To get a better understanding of the local behavior of the proposed TDV regularizer, we perform a nonlinear eigenfunction analysis [16]. To this end, we compute *nonlinear eigenfunctions* by minimizing the variational problem

$$\min_{x \in [0,1]^{nC}} \frac{1}{2} \|D_1R(x, \theta) - \Lambda(x)x\|_2^2, \quad (12)$$

where the generalized Rayleigh quotient defining the *eigenvalues* is given by

$$\Lambda(x) = \frac{\langle D_1R(x, \theta), x \rangle}{\|x\|_2^2}.$$

Note that (12) enforces $D_1R(x, \theta) \approx \Lambda(x)x$ for images with range space $[0, 1]$. We use Nesterov’s projected accelerated gradient descent [36] to perform the optimization in (12). Due to the nonconvexity of this minimization problem the resulting eigenfunctions strongly depend on the initialization.

Figure 8 depicts six images from the BSDS400 dataset (first row), which are used as the initialization, along with their eigenfunctions for gray-scale denoising (second row, $\sigma = 25$), color denoising (third row, $\sigma = 25$) and SISR (last row, $\gamma = 2$ and $\sigma = 0$). For denoising (second and third row), the generated eigenfunctions are composed of piecewise constant regions with smooth edges resulting in cartoon-like simplifications and contrast enhancement (see e.g. second/third column). Textured regions of the initial image are transformed into repetitive structures such as stripes and dots. In contrast, the eigenfunctions for SISR (fourth column) exhibit fine-scaled texture details, which explain the property of the learned regularizer to recover high-frequencies. These results clearly demonstrate that the learned TDV regularizers are discriminative priors as they adapt to specific image reconstruction tasks.

5.7 Stability Analysis

In what follows, we elaborate on the stability of the proposed approach w.r.t. perturbations of the initial image and the learned parameters of TDV. To this end, we numerically analyze the local structure of the regularization energy and experimentally validate Theorem 4.1 and Theorem 4.2. In all experiments in this subsection, we use the TDV_3^3 regularizer.

Let $x \in \mathbb{R}^{nC}$ be an image, $\xi \sim \mathcal{N}(0, \sigma^2 \text{Id})$ and θ parameters trained for gray-scale Gaussian denoising with $\sigma = 25$. Figure 9 visualizes the surface plots of the pointwise deep variation $[-1, 1] \ni (\zeta_1, \zeta_2) \mapsto r(\zeta_1 x + \zeta_2 \xi, \theta)_i$ as a function of the contrast ζ_1 and the noise level ζ_2 for four prototypic pixels i marked in red. All surface plots exhibit distinct global minima and no high-frequency oscillations can be observed. Moreover, the pointwise deep variation strictly increases from the origin in all directions.

Motivated by the aforementioned surface plots, we can now conduct the stability analysis w.r.t. perturbations of the input. For this purpose, we estimate quantiles of the local Lipschitz constants L_x and L_θ of TDV by uniformly drawing 10^5 patches of size 128×128 from the BSDS400 dataset. To this end, we consider an image patch y randomly drawn from the BSDS68 dataset and let $\xi, \tilde{\xi}$ be two noise instances independently drawn from $\mathcal{N}(0, \sigma^2 \text{Id})$ for $\sigma = 25$. The associated observations are denoted by $z = y + \xi$ and $\tilde{z} = y + \tilde{\xi}$, resulting in the states x_s and \tilde{x}_s . Figure 10 (upper left) depicts the normalized norm differences $\frac{1}{nC} \|x_s - \tilde{x}_s\|_2$ for all 68 patches (light blue curves), the corresponding mean curve (blue curve) as well as the upper bounds obtained from Theorem 4.1 for $\delta = 0.5$ (orange curve) and $\delta = 0.05$ (green curve) for gray-scale additive Gaussian denoising as a function of s . It



Figure 8: First row: initial images taken from BSDS400 dataset. Second to fourth row: corresponding eigenfunctions for gray-scale denoising (second row, $\sigma = 25$), color denoising (third row, $\sigma = 25$) and SISR (last row, $\gamma = 2$ and $\sigma = 0$).

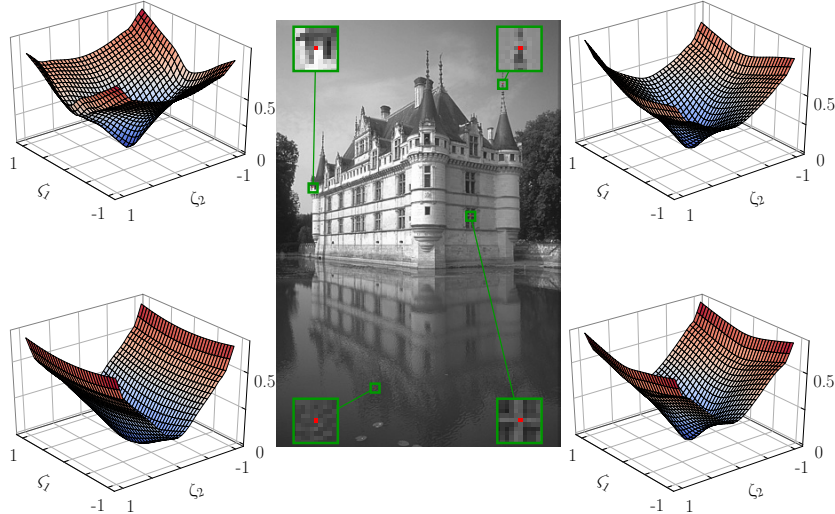


Figure 9: Surface plots of the pointwise deep variation $[-1, 1] \ni (\zeta_1, \zeta_2) \mapsto r(\zeta_1 x + \zeta_2 \xi, \theta)_i$ of four patches—each evaluated at the red center pixel.

turns out that the normalized norm differences along the trajectories are only slightly overestimated. Furthermore, the normalized norm differences strictly monotonically decrease for increasing s , which is also reflected in the upper bounds due to $\alpha_1(\delta) < 1$.

Next, we elaborate on the stability analysis w.r.t. variations of the learned parameters. Let y be a randomly drawn 128×128 -patch from the BSDS68 dataset, which is corrupted by additive Gaussian noise ξ with $\sigma = 25$, i.e. $z = y + \xi$. We consider optimized parameters $\theta \in \Theta$ for gray-scale Gaussian denoising. The TDV parameters $\tilde{\theta}$ satisfies $\tilde{\theta} \sim \mathcal{U}(\text{proj}_{\Theta}(B_{\epsilon}(\theta)))$ with $\epsilon = 0.1$. Hence, $\tilde{\theta}$ is the element-wise sum of θ and strong uniform noise in the relative ϵ -ball around θ . We denote by x_s and \tilde{x}_s two states associated with θ and $\tilde{\theta}$ emanating from the same noisy observation z . In Figure 10 (lower left), the normalized norm differences of the states x_s and \tilde{x}_s for all 68 patches (light blue curves), the corresponding mean curve (blue curve) as well as the theoretical upper bounds derived in Theorem 11 for $\delta = 0.5$ (orange curve) and $\delta = 0.05$ (green curve) are plotted as a function of s . As a result, the upper bound for $\delta = 0.5$ for $s = 10$ is roughly four times higher than the expected curve of the normalized norm differences.

In the case of SISR for $\gamma = 3$ and $\sigma = 7.65$, the results of the stability analysis are depicted on the right side of Figure 10. Here, the theoretical upper bounds are less tight compared to Gaussian denoising due to the inclusion of the non-trivial linear operators A with a non-empty nullspace and A_{init} with $\|A_{\text{init}}\|_2 = \gamma$. Note that the solutions of SISR are not unique due to the structure of A .

To conclude, in all four cases the normalized norm differences (blue curves) are almost flat and the band width only slightly increases with s . This numerically validates that the proposed method is robust w.r.t. variations of both the observations and the learned parameters.

5.8 Robustness against Adversarial Attacks

In what follows, we numerically check the robustness of the proposed method against adversarial attacks of the TDV₃ regularizer trained for gray-scale Gaussian denoising with $\sigma = 25$. Let $y \in \mathbb{R}^{nC}$

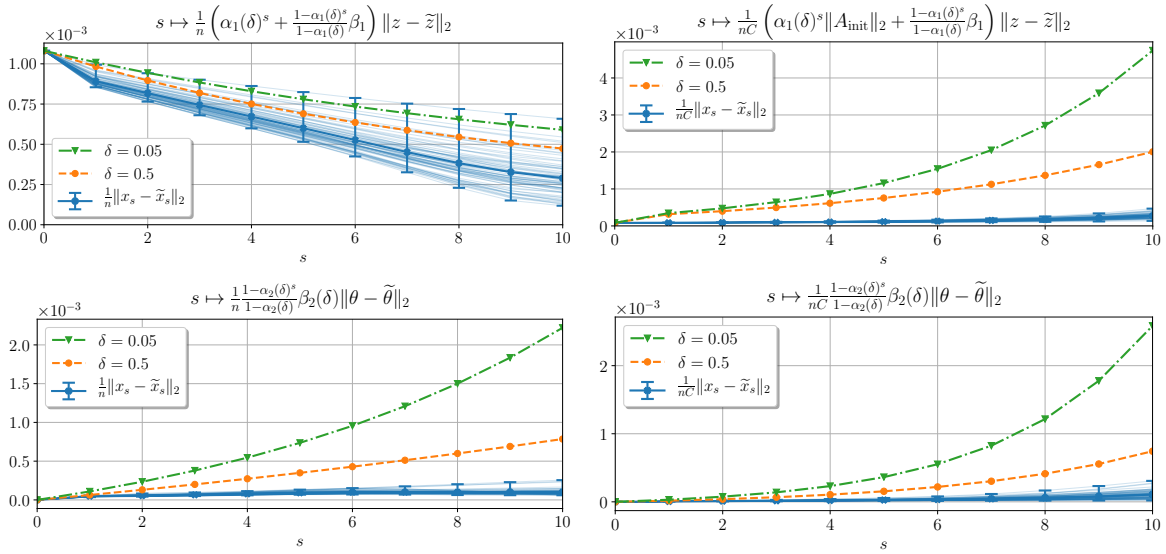


Figure 10: First row: stability analysis w.r.t. input of the proposed approach for gray-scale Gaussian denoising (left) trained for $\sigma = 25/S = 10$ and SISR (right) with $\gamma = 3/\sigma = 7.65/S = 10$. Second row: stability analysis w.r.t. the learned TDV₃ parameters for gray-scale Gaussian denoising (left) and SISR (right).

be a ground truth image patch, $\xi \sim \mathcal{N}(0, \sigma^2 \text{Id})$ Gaussian noise and $z = y + \xi \in \mathbb{R}^l$. The adversarial noise $\tilde{\xi}$ for $\epsilon > 0$ is computed via

$$\max_{\tilde{\xi} \in \mathbb{R}^l: \|\tilde{\xi}\|_2 \leq \epsilon} \|\hat{x}_S(y, \xi + \tilde{\xi}, T, \theta) - y\|_2^2.$$

Thus, we seek the noise structure that leads to the largest deviation from y around z .

Figure 11 shows two different ground truth image patches, the corresponding restored images along with the computed adversarial noise structures and corresponding output images for $\epsilon \in \{1, 2\}$. As a result, with increasing ϵ high-frequency patterns (dotted and striped structures) are generated in the adversarial noise, which are emphasized in the corresponding output images. Moreover, we observe high-frequency local noise patterns in both reconstructed images for $\epsilon = 2$. In particular, no new structures are hallucinated, only existing patterns are intensified in $x_S(\tilde{\xi})$.

5.9 Empirical Upper Bound for Generalization Error

Next, we experimentally compute worst case upper bounds for the generalization error of the TDV₃ regularizer trained for gray-scale Gaussian denoising with $\sigma = 25$. As a starting point, let $\mathcal{Y} \subset [0, 1]^n$ be the set of natural images with distribution $\mathcal{T}_{\mathcal{Y}}$. Further, let $\mathcal{Y}' \subset \mathcal{Y}$ be a collection of 10^5 ground truth image patches of size 128×128 randomly drawn from the BSDS400 dataset, the BSDS68 dataset, and the DIV2K validation set [1]. The uniform distribution on \mathcal{Y}' is denoted by $\mathcal{T}_{\mathcal{Y}'}$. Following [4],

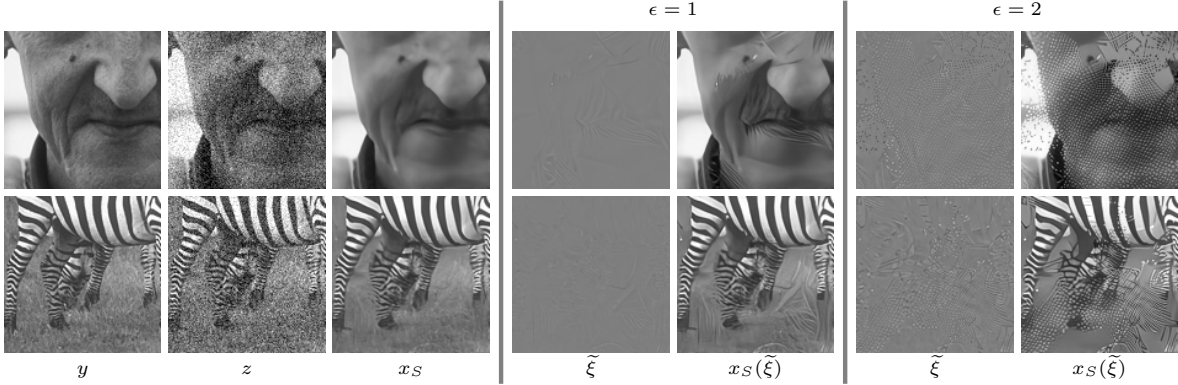


Figure 11: From left to right: ground truth image patch y (first column), noisy observation $z = y + \xi$ (second column), reconstructed image (third column), pairs of (adversarial) noise and resulting output for radii $\epsilon = 1$ (fourth/fifth column) and $\epsilon = 2$ (sixth/seventh column), where $x_S(\tilde{\xi}) = \hat{x}_S(y, \xi + \tilde{\xi}, T, \theta)$. The adversarial noise $\tilde{\xi}$ is displayed in the range $[-0.5, 0.5]$.

the *empirical risk* w.r.t. \mathcal{Y}' is defined as

$$E_{\text{emp}}(\mathcal{Y}') := \frac{1}{|\mathcal{Y}'|} \sum_{y' \in \mathcal{Y}'} \ell(\hat{x}_S(y', \xi_{y'}) - y'),$$

the *expected loss* of \mathcal{Y} reads as

$$E(\mathcal{Y}) := \mathbb{E}_{y \sim \mathcal{T}_Y} \ell(\hat{x}_S(y, \xi_y) - y),$$

where $\ell(x) = \|x\|_2^2$, ξ_y and $\xi_{y'}$ are a priori sampled noise instances drawn from $\mathcal{N}(0, \sigma^2 \text{Id})$, and $\hat{x}_S(y, \xi) = \hat{x}_S(y, \xi, T, \theta)$. In this case, the *generalization error* for \mathcal{Y}' is defined as $|E(\mathcal{Y}) - E_{\text{emp}}(\mathcal{Y}')|$. A worst case upper bound for this generalization error is given by

$$\max_{\tilde{y} \in [0, 1]^n} \ell(\hat{x}_S(\tilde{y}, \xi) - \tilde{y}) - E_{\text{emp}}(\mathcal{Y}') \quad (13)$$

for an a priori sampled $\xi \sim \mathcal{N}(0, \sigma^2 \text{Id})$ since the expected loss is estimated from above by its single worst realization.

To analyze the dependency between $\ell(\hat{x}_S(y', \xi_{y'}) - y')$ and the regularization energy $R(y', \theta)$, we show a scatter plot of the corresponding plane in Figure 12 (left) for all $y' \in \mathcal{Y}'$. We observe a strikingly linear dependency, which is reflected by an R^2 -value of 0.985 of a linear regression with intercept. This linear dependency gives rise to a probabilistic analysis of worst case upper bounds for the generalization error on quantiles of the regularization energy. For this reason, we define the cumulative distribution function

$$F_R(H) = \mathbb{P}(R(y', \theta) \leq H : y' \sim \mathcal{T}_{Y'})$$

for $H \in \mathbb{R}$. Note that $F_R^{-1}(q)$ for $q \in (0, 1]$ defines the q^{th} -quantile of the regularization energy over \mathcal{Y}' . Then, we derive an upper bound for the generalization error restricted to the subset

$$\mathcal{Y}'_q = \{y' \in \mathcal{Y}' : R(y', \theta) \leq F_R^{-1}(q)\}$$

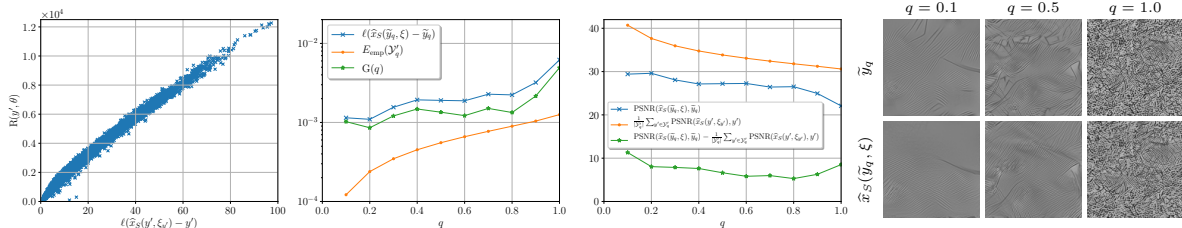


Figure 12: First plot: scatter plot in the $\ell(\widehat{x}_S(y, \xi_y) - y)$ and $R(y, \theta)$ -plane. Second plot: semi-logarithmic plots of the upper bound for expected loss (blue curve), the empirical risk (orange curve) and the upper bound for the generalization error (green curve) restricted to \mathcal{Y}'_q as a function of the quantiles q . Third plot: corresponding PSNR curves measured in dB. Right: pairs of worst case ground truth \tilde{y}_q and corresponding output image $\widehat{x}_S(\tilde{y}_q, \xi)$ for $q = 0.1, 0.5, 1.0$.

for $q \in (0, 1]$. In this setting, the expected loss of the q^{th} -quantile is estimated from above by $\ell(\widehat{x}_S(\tilde{y}_q) - \tilde{y}_q)$, where

$$\tilde{y}_q \in \underset{y \in [0, 1]^n}{\operatorname{argmax}} \ell(\widehat{x}_S(y, \xi) - y) \quad \text{s.t.} \quad R(y) \leq F_R^{-1}(q). \quad (14)$$

In detail, we try to identify the image patch \tilde{y}_q that leads to the worst case loss ℓ among all image patches in $[0, 1]^n$ such that their regularization energy $R(\tilde{y}_q)$ is at most $F_R^{-1}(q)$. Hence, an upper bound for the generalization error on the set \mathcal{Y}'_q is given by

$$G(q) := \ell(\widehat{x}_S(\tilde{y}_q, \xi) - \tilde{y}_q) - E_{\text{emp}}(\mathcal{Y}'_q).$$

To compute the worst case ground truth image, we account for the constraint in (14) by a quadratic barrier approach and solve the resulting minimization problem using Nesterov's accelerated gradient method [36] with Lipschitz backtracking starting from a patch with uniform noise.

Figure 12 (second plot) depicts the semi-logarithmic plots of the upper bound for the empirical risk (blue curve), the empirical risk (orange curve), and the upper bound for the generalization error (green curve) on the set \mathcal{Y}'_q depending on q . For convenience, the third plot depicts corresponding PSNR curves measured in dB. We note that the upper bound for the generalization error slightly increases with larger regularization energy values represented by larger q . We observe that the upper bound is not tight, which originates from the minimization in (14) among all patches in $[0, 1]^n$. The computed worst case patches \tilde{y}_q along with the reconstructed output images $\widehat{x}_S(\tilde{y}_q, \xi)$ are shown in Figure 12 (right). For low values of q the worst case ground truth patches consist of high-oscillatory stripe patterns and checkerboard artifacts, whereas noise and texture patterns are dominant for higher values of q . We emphasize that all generated patches are artificial and not likely to be contained in any natural image, that is why the upper bound for generalization error has a tendency to overestimate the actual generalization error.

6 Conclusion

The proposed total deep variation regularizer is motivated by established deep network architectures. Moreover, the inherent variational structure of our approach enables a rigorous mathematical understanding encompassing an optimality condition for optimal stopping, and a nonlinear eigenfunction

analysis. We have derived theoretical upper bounds for the stability analysis, which led to relatively tight bounds in the numerical experiments. For image denoising and single image super-resolution, our model generates state-of-the-art results with an impressively low number of trainable parameters. To underline the versatility of TDV for generic linear inverse problems, we successfully demonstrated their applicability for the challenging CT and MRI reconstruction tasks without requiring any additional training. Finally, we have conducted adversarial attacks and an empirical worst case generalization error analysis to demonstrate the robustness of our approach.

Acknowledgments

The authors acknowledge support from the ERC starting grant HOMOVIS (No. 640156) and ERC advanced grant OCLOC (No. 668998).

References

- [1] Eirikur Agustsson and Radu Timofte. NTIRE 2017 challenge on single image super-resolution: Dataset and study. In *IEEE Conference on Computer Vision and Pattern Recognition Workshops*, 2017.
- [2] Luigi Ambrosio, Nicola Gigli, and Giuseppe Savaré. *Gradient flows in metric spaces and in the space of probability measures*. Lectures in Mathematics ETH Zürich. Birkhäuser Verlag, Basel, second edition, 2008.
- [3] Vegard Antun, Francesco Renna, Clarice Poon, Ben Adcock, and Anders C. Hansen. On instabilities of deep learning in image reconstruction and the potential costs of ai. *Proceedings of the National Academy of Sciences*, 2020.
- [4] Olivier Bousquet and André Elisseeff. Stability and generalization. *J. Mach. Learn. Res.*, 2(3):499–526, 2002.
- [5] Kristian Bredies, Karl Kunisch, and Thomas Pock. Total generalized variation. *SIAM J. Imaging Sci.*, 3(3):492–526, 2010.
- [6] Antonin Chambolle and Pierre-Louis Lions. Image recovery via total variation minimization and related problems. *Numer. Math.*, 76(2):167–188, 1997.
- [7] Antonin Chambolle and Thomas Pock. An introduction to continuous optimization for imaging. *Acta Numer.*, 25:161–319, 2016.
- [8] Antonin Chambolle and Thomas Pock. Total roto-translational variation. *Numer. Math.*, 142(3):611–666, 2019.
- [9] Tony F. Chan, Sung Ha Kang, and Jianhong Shen. Euler’s elastica and curvature-based inpainting. *SIAM J. Appl. Math.*, 63(2):564–592, 2002.
- [10] Guang-Hong Chen, Jie Tang, and Shuai Leng. Prior image constrained compressed sensing (PICCS): A method to accurately reconstruct dynamic CT images from highly undersampled projection data sets. *Medical Physics*, 35(2):660–663, 2008.

- [11] Yunjin Chen and Thomas Pock. Trainable nonlinear reaction diffusion: A flexible framework for fast and effective image restoration. *IEEE Transactions on Pattern Analysis and Machine Intelligence*, 39(6):1256–1272, 2017.
- [12] Kostadin Dabov, Alessandro Foi, Vladimir Katkovnik, and Karen Egiazarian. Image denoising by sparse 3-D transform-domain collaborative filtering. *IEEE Transactions on Image Processing*, 16(8):2080–2095, 2007.
- [13] Justin Domke. Generic methods for optimization-based modeling. In *International Conference on Artificial Intelligence and Statistics*, pages 318–326, 2012.
- [14] Weinan E, Jiequn Han, and Qianxiao Li. A mean-field optimal control formulation of deep learning. *Res. Math. Sci.*, 6(1):Paper No. 10, 41, 2019.
- [15] Alexander Effland, Erich Kobler, Karl Kunisch, and Thomas Pock. Variational Networks: An Optimal Control Approach to Early Stopping Variational Methods for Image Restoration. *J. Math. Imaging Vision*, 62(3):396–416, 2020.
- [16] Guy Gilboa. *Nonlinear eigenproblems in image processing and computer vision*. Advances in Computer Vision and Pattern Recognition. Springer, Cham, 2018.
- [17] Ian J Goodfellow, Jonathon Shlens, and Christian Szegedy. Explaining and harnessing adversarial examples. In *International Conference on Learning Representations*, 2015.
- [18] Sungsoo Ha and Klaus Mueller. A look-up table-based ray integration framework for 2-D/3-D forward and back projection in X-ray CT. *IEEE Transactions on Medical Imaging*, 37:361–371, 2018.
- [19] Kerstin Hammernik, Teresa Klatzer, Erich Kobler, Michael P. Recht, Daniel K. Sodickson, Thomas Pock, and Florian Knoll. Learning a variational network for reconstruction of accelerated MRI data. *Magnetic Resonance in Medicine*, 79(6):3055–3071, 2018.
- [20] Xiangyu He, Zitao Mo, Peisong Wang, Yang Liu, Mingyuan Yang, and Jian Cheng. ODE-inspired network design for single image super-resolution. In *IEEE Conference on Computer Vision and Pattern Recognition*, pages 1732–1741, 2019.
- [21] Jingsang Huang and David Mumford. Statistics of natural images and models. In *IEEE Conference on Computer Vision and Pattern Recognition*, pages 541–547, 1999.
- [22] Xixi Jia, Sanyang Liu, Xiangchu Feng, and Lei Zhang. FOCNet: A fractional optimal control network for image denoising. In *IEEE Conference on Computer Vision and Pattern Recognition*, pages 6047–6056, 2019.
- [23] Jiwon Kim, Jung Kwon Lee, and Kyoung Mu Lee. Accurate image super-resolution using very deep convolutional networks. In *IEEE Conference on Computer Vision and Pattern Recognition*, pages 1646–1654, 2016.
- [24] Diederik P. Kingma and Jimmy Lei Ba. ADAM: a method for stochastic optimization. In *International Conference on Learning Representations*, 2015.
- [25] Erich Kobler, Alexander Effland, Karl Kunisch, and Thomas Pock. Total deep variation for linear inverse problems. In *IEEE Conference on Computer Vision and Pattern Recognition*, 2020.

- [26] Erich Kobler, Teresa Klatzer, Kerstin Hammernik, and Thomas Pock. Variational networks: Connecting variational methods and deep learning. In *German Conference on Pattern Recognition*, pages 281–293. Springer International Publishing, 2017.
- [27] Stamatios Lefkimmiatis. Non-local color image denoising with convolutional neural networks. In *IEEE Conference on Computer Vision and Pattern Recognition*, pages 5882–5891, 2016.
- [28] Anat Levin and Boaz Nadler. Natural image denoising: Optimality and inherent bounds. In *IEEE Conference on Computer Vision and Pattern Recognition*, pages 2833–2840, 2011.
- [29] Housen Li, Johannes Schwab, Stephan Antholzer, and Markus Haltmeier. NETT: solving inverse problems with deep neural networks. *Inverse Problems*, 2020.
- [30] Sebastian Lunz, Ozan Öktem, and Carola-Bibiane Schönlieb. Adversarial regularizers in inverse problems. In *Advances in Neural Information Processing Systems*, pages 8507–8516, 2018.
- [31] David Martin, Charless Fowlkes, Doron Tal, and Jitendra Malik. A database of human segmented natural images and its application to evaluating segmentation algorithms and measuring ecological statistics. In *IEEE International Conference on Computer Vision*, pages 416–423, 2001.
- [32] Cynthia H. McCollough, Adam C. Bartley, Rickey E. Carter, Baiyu Chen, Tammy A. Drees, Phillip Edwards, David R. Holmes III, Alice E. Huang, Farhana Khan, Shuai Leng, Kyle L. McMillan, Gregory J. Michalak, Kristina M. Nunez, Lifeng Yu, and Joel G. Fletcher. Low-dose CT for the detection and classification of metastatic liver lesions: Results of the 2016 low dose CT grand challenge. *Medical Physics*, 44(10):339–352, 2017.
- [33] Tim Meinhardt, Michael Möller, Caner Hazirbas, and Daniel Cremers. Learning proximal operators: Using denoising networks for regularizing inverse imaging problems. In *IEEE International Conference on Computer Vision*, pages 1781–1790, 2017.
- [34] Seyed-Mohsen Moosavi-Dezfooli, Alhussein Fawzi, Omar Fawzi, and Pascal Frossard. Universal adversarial perturbations. In *IEEE Conference on Computer Vision and Pattern Recognition*, pages 1765–1773, 2017.
- [35] Seyed-Mohsen Moosavi-Dezfooli, Alhussein Fawzi, and Pascal Frossard. Deepfool: a simple and accurate method to fool deep neural networks. In *IEEE Conference on Computer Vision and Pattern Recognition*, pages 2574–2582, 2016.
- [36] Yuri E. Nesterov. A method of solving a convex programming problem with convergence rate $\mathcal{O}(\frac{1}{k^2})$. *Dokl. Akad. Nauk SSSR*, 269(3):543–547, 1983.
- [37] Andrew Y. Ng and Michael I. Jordan. On discriminative vs. generative classifiers: A comparison of logistic regression and naive Bayes. In *Advances in Neural Information Processing Systems 14*, pages 841–848. MIT Press, 2002.
- [38] Mark Nitzberg, David Mumford, and Takahiro Shiota. *Filtering, segmentation and depth*, volume 662 of *Lecture Notes in Computer Science*. Springer-Verlag, Berlin, 1993.
- [39] Tobias Plötz and Stefan Roth. Neural nearest neighbors networks. In *Advances in Neural Information Processing Systems 31*, pages 1087–1098. Curran Associates, Inc., 2018.

- [40] J. H. Rick Chang, Chun-Liang Li, Barnábas Póczos, B. V. K. Vijaya Kumar, and Aswin C. Sankaranarayanan. One network to solve them all — solving linear inverse problems using deep projection models. In *IEEE International Conference on Computer Vision*, pages 5888–5897, 2017.
- [41] Yaniv Romano, Michael Elad, and Peyman Milanfar. The little engine that could: regularization by denoising (RED). *SIAM J. Imaging Sci.*, 10(4):1804–1844, 2017.
- [42] Olaf Ronneberger, Philipp Fischer, and Thomas Brox. U-Net: Convolutional networks for biomedical image segmentation. In *Medical Image Computing and Computer-Assisted Intervention*, pages 234–241. Springer, 2015.
- [43] Stefan Roth and Michael J. Black. Fields of Experts. *Int. J. Comput. Vis.*, 82(2):205–229, 2009.
- [44] Leonid I. Rudin, Stanley Osher, and Emad Fatemi. Nonlinear total variation based noise removal algorithms. *Phys. D*, 60(1-4):259–268, 1992.
- [45] Kegan G. G. Samuel and Marshall F. Tappen. Learning optimized MAP estimates in continuously-valued MRF models. In *IEEE Conference on Computer Vision and Pattern Recognition*, pages 477–484, 2009.
- [46] Christian Szegedy, Wojciech Zaremba, Ilya Sutskever, Joan Bruna, Dumitru Erhan, Ian Goodfellow, and Rob Fergus. Intriguing properties of neural networks. In *International Conference on Learning Representations*, 2014.
- [47] Ying Tai, Jian Yang, and Xiaoming Liu. Image super-resolution via deep recursive residual network. In *IEEE Conference on Computer Vision and Pattern Recognition*, pages 2790–2798, 2017.
- [48] Ying Tai, Jian Yang, Xiaoming Liu, and Chunyan Xu. MemNet: A persistent memory network for image restoration. In *IEEE International Conference on Computer Vision*, pages 4549–4557, 2017.
- [49] Gerald Teschl. *Ordinary differential equations and dynamical systems*, volume 140 of *Graduate Studies in Mathematics*. American Mathematical Society, Providence, RI, 2012.
- [50] Martin Uecker, Peng Lai, Mark J. Murphy, Patrick Virtue, Michael Elad, John M. Pauly, Shreyas S. Vasanawala, and Michael Lustig. ESPIRiT: an eigenvalue approach to autocalibrating parallel MRI: where SENSE meets GRAPPA. *Magnetic Resonance in Medicine*, 71(3):990–1001, 2014.
- [51] Singanallur V. Venkatakrishnan, Charles A. Bouman, and Brendt Wohlberg. Plug-and-play priors for model based reconstruction. In *IEEE Global Conference on Signal and Information Processing*, pages 945–948, 2013.
- [52] Eberhard Zeidler. *Nonlinear functional analysis and its applications. III*. Springer-Verlag, New York, 1985.
- [53] Kai Zhang, Luc Van Gool, and Radu Timofte. Deep unfolding network for image super-resolution. *arXiv:2003.10428*, 2020.

- [54] Kai Zhang, Wangmeng Zuo, Yunjin Chen, Deyu Meng, and Lei Zhang. Beyond a Gaussian denoiser: Residual learning of deep CNN for image denoising. *IEEE Transactions on Image Processing*, 26(7):3142–3155, 2017.
- [55] Kai Zhang, Wangmeng Zuo, and Lei Zhang. FFDNet: Toward a fast and flexible solution for CNN-based image denoising. *IEEE Transactions on Image Processing*, 27(9):4608–4622, 2018.
- [56] Richard Zhang. Making convolutional networks shift-invariant again. In *International Conference on Machine Learning*, 2019.
- [57] Ningning Zhao, Qi Wei, Adrian Basarab, Nicolas Dobigeon, Denis Kouamé, and Jean-Yves Tourneret. Fast single image super-resolution using a new analytical solution for ℓ_2 - ℓ_2 problems. *IEEE Trans. Image Process.*, 25(8):3683–3697, 2016.
- [58] Song Chun Zhu, Yingnian Wu, and David Mumford. Filters, random fields and maximum entropy (FRAME): Towards a unified theory for texture modeling. *Int. J. Comput. Vision*, 27(2):107–126, 1998.